Earth and Planetary Science Letters 451 (2016) 138–148

Contents lists available at ScienceDirect

Earth and Planetary Science Letters

www.elsevier.com/locate/epsl

Testing the limits in a greenhouse ocean: Did low nitrogen availability limit marine productivity during the end-Triassic mass extinction?

Shane D. Schoepfer [a,*], Thomas J. Algeo [b,c], Peter D. Ward [d], Kenneth H. Williford [e], James W. Haggart [f]

[a] Department of Geoscience, University of Calgary, Calgary, AB T2N 1N4 Canada
[b] Department of Geology, University of Cincinnati, Cincinnati, OH 45221, USA
[c] State Key Laboratories of Biogeology and Environmental Geology and Geological Processes and Mineral Resources, China University of Geosciences, Wuhan 430074, China
[d] Department of Biology, University of Washington, Seattle, WA 98195, USA
[e] Jet Propulsion Laboratory, California Institute of Technology, Pasadena, CA 91109, USA
[f] Geological Survey of Canada–Vancouver, Vancouver, British Columbia V6B 5J3, Canada

ARTICLE INFO

Article history:
Received 9 January 2016
Received in revised form 17 June 2016
Accepted 26 June 2016
Available online xxxx
Editor: M. Frank

Keywords:
Triassic
Jurassic
euxinia
Panthalassic
ammonium
Wrangellia

ABSTRACT

The end-Triassic mass extinction has been characterized as a 'greenhouse extinction', related to rapid atmospheric warming and associated changes in ocean circulation and oxygenation. The response of the marine nitrogen cycle to these oceanographic changes, and the extent to which mass extinction intervals represent a deviation in nitrogen cycling from other ice-free 'greenhouse' periods of Earth history, remain poorly understood. The well-studied Kennecott Point section in Haida Gwaii, British Columbia, Canada, was deposited in the open Panthalassic Ocean, and is used here as a test case to better understand changes in the nitrogen cycle and marine productivity from the pre-crisis greenhouse of the Rhaetian to the latest-Rhaetian crisis interval. We estimated marine productivity from the late Norian to the early Hettangian using TOC- and P-based paleoproductivity transform equations, and then compared these estimates to records of sedimentary nitrogen isotopes, redox-sensitive trace elements, and biomarker data. Major negative excursions in $\delta^{15}N$ (to $\leq 0‰$) correspond to periods of depressed marine productivity. During these episodes, the development of a stable pycnocline below the base of the photic zone suppressed vertical mixing and limited N availability in surface waters, leading to low productivity and increased nitrogen fixation, as well as ecological stresses in the photic zone. The subsequent shoaling of euxinic waters into the ocean surface layer was fatal for most Triassic marine fauna, although the introduction of regenerated NH_4^+ into the photic zone may have allowed phytoplankton productivity to recover. These results indicate that the open-ocean nitrogen cycle was influenced by climatic changes during the latest Triassic, despite having existed in a greenhouse state for over 50 million years previously, and that low N availability limited marine productivity for hundreds of thousands of years during the end-Triassic crisis.

1. Introduction

The end-Triassic mass extinction (ETME), ~201.6 million years ago (Blackburn et al., 2013), was among the most severe of the Phanerozoic, impacting both terrestrial and marine faunas. As with the end-Permian event, the end-Triassic extinction has been linked to a major flood basalt eruption, that of the Central Atlantic Magmatic Province (CAMP), which was associated with the opening of the North Atlantic in the Late Triassic to Early Jurassic. The recent study by Blackburn et al. (2013) inferred a strong correlation between the onset of CAMP volcanism and terminal Triassic extinctions in the incipient Atlantic basin.

In the 'greenhouse extinction' scenario (Kump et al., 2005; Kidder and Worsley, 2010), rapid warming of the oceans and atmosphere drives a cascade of environmental and ecological effects, including ocean stratification leading to deepwater anoxia (Fig. 1; Kump et al., 2005; Richoz et al., 2012), enhanced terrestrial erosion and sediment flux to the oceans (Algeo and Twitchett, 2010), methane clathrate destabilization driving a positive warming feedback (Kidder and Worsley, 2010), ocean acidification (Črne et al., 2011), and prolonged instability in marine nutrient cycles, produc-

* Corresponding author.
E-mail address: shane.schoepfer@ucalgary.ca (S.D. Schoepfer).

http://dx.doi.org/10.1016/j.epsl.2016.06.050
0012-821X/

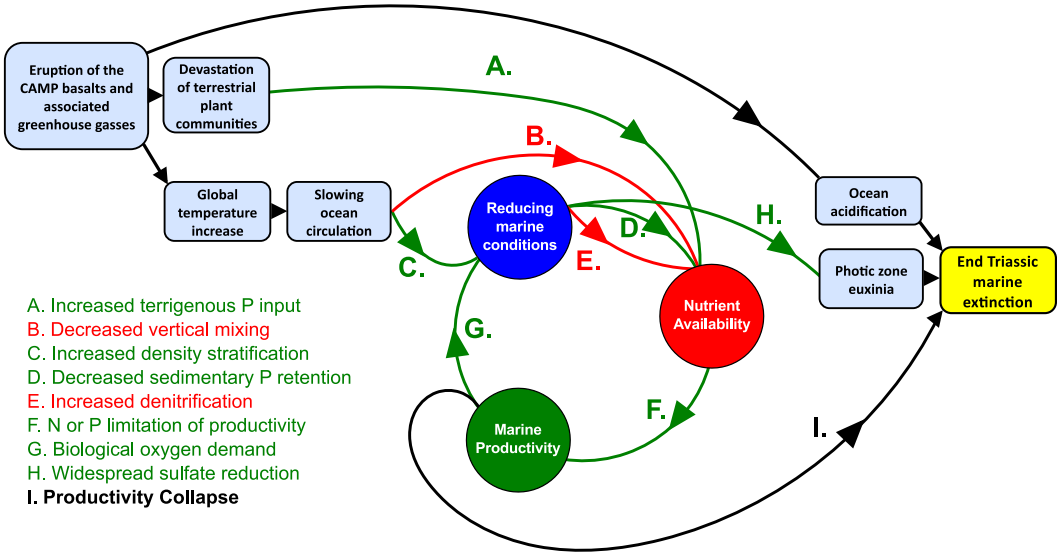

Fig. 1. Schematic flowchart of the 'greenhouse extinction' model for the ETME, highlighting the complex relationship between nutrient availability, primary productivity, and redox conditions. Positive feedback relationships between factors are shown in green, and negative feedback relationships in red; black arrows indicate direct causal relationships that do not rely on feedback mechanisms. Letters refer to legend in lower left corner of figure. (For interpretation of the references to color in this figure legend, the reader is referred to the web version of this article.)

tivity rates, and organic carbon burial fluxes (Whiteside and Ward, 2011). Biomarker studies have documented water-column stratification and euxinia in many sections globally (Richoz et al., 2012; van de Schootbrugge et al., 2013; Kasprak et al., 2015), although the specific mechanisms by which greenhouse warming disturbed marine biogeochemical cycles are not yet clear.

This study uses the expanded, biostratigraphically well-studied Kennecott Point section in Haida Gwaii, British Columbia (Ward et al., 2001, 2004; Williford et al., 2007, 2009; Kasprak et al., 2015) as a test case to examine how marine nutrient cycles respond to major climatic warming events, and the effects of these nutrient cycle disturbances on marine productivity. As productivity is among the most important factors determining marine redox conditions, and the redox environment in turn affects nutrient cycles through denitrification (Algeo et al., 2014) and phosphate retention in sediments (Ingall et al., 2005), these three factors form an interconnected loop (Fig. 1), with the behavior of nitrogen in dysoxic greenhouse oceans governing whether this loop behaves as an accelerating positive or stabilizing negative feedback.

The difficulty of assessing the N cycle during mass extinction intervals is compounded by the fact that many mass extinctions (including the ETME) took place during extended periods without permanent polar ice. While representing the "normal" backdrop against which catastrophic losses in biodiversity must be measured, such greenhouse worlds may have had radically different patterns of nitrogen cycling than those seen in the modern icehouse ocean. A recently published compilation of Phanerozoic nitrogen isotope data demonstrated a major change in modality between icehouse and greenhouse intervals, with the predominantly low sedimentary nitrogen isotope ($\delta^{15}N$) values during greenhouse periods attributed to an expanded role of sedimentary denitrification on flooded continental shelves (Algeo et al., 2014). Nevertheless, rapid negative deviations from this baseline greenhouse state are observed at the ETME (Richoz et al., 2012; Kasprak et al., 2015), when permanent polar ice was already long absent, and are thus unlikely to reflect an increase in flooded continental shelf area.

Denitrification in the global ocean is hypothesized to have increased during greenhouse intervals and to have been balanced by increased cyanobacterial N fixation (Kidder and Worsley, 2010), although it is unclear if this would have had any net effect on global marine productivity. The prevailing view of nutrient limitation in the modern oceans is that, whereas bioavailable N limits phytoplankton growth on short timescales, diazotrophs are able to fix enough N from the atmosphere to maintain a Redfieldian balance with phosphorus over longer timescales (Tyrrell, 1999). It is an open question, however, whether diazotrophs were able to "keep pace" with nitrogen depletion through denitrification in a greenhouse regime, and decreases in marine productivity have been attributed to pervasive N limitation during warm intervals of Earth history (Saltzman, 2005).

Productivity has often been viewed as a first order control on species diversity at geologic time scales (Allmon and Martin, 2014). However, high abundances of a few species have been used to infer eutrophic, nutrient-rich conditions locally, based on the assumption that abundant nutrients favor opportunistic species best able to utilize them and exclude competitors (Brasier, 1995). During the ETME crisis, both increased and decreased primary productivity have been inferred (Ward et al., 2001; Richoz et al., 2012; van de Schootbrugge et al., 2013), although the potentially restricted nature of the incipient North Atlantic Ocean may have been at least partially responsible for differences between European sections and the open Panthalassic Ocean. Reconciling the contradictions between these results through the application of more quantitative paleoproductivity estimates is a major aim of the present study.

2. Geologic background

The Haida Gwaii archipelago (formerly Queen Charlotte Islands) of British Columbia is part of the exotic Wrangellia Terrane (Fig. 2; Jones et al., 1977), which originated as an offshore volcanic arc during the late Paleozoic, and was engulfed within a large basaltic plateau emplaced during the Triassic (Greene et al., 2010). Although the latitude of Wrangellia and its position relative to North America prior to accretion are subjects of ongoing research, it is likely that the study units were deposited at a lower paleolatitude than their current location (Housen and Beck, 1999). Upper Triassic sedimentary strata are interpreted as having been deposited in an outer shelf to slope environment (~200–500 m water depth; Haggart et al., 2001). The abundant radiolarian fauna is similar in taxonomic composition to those from accreted abyssal cherts in

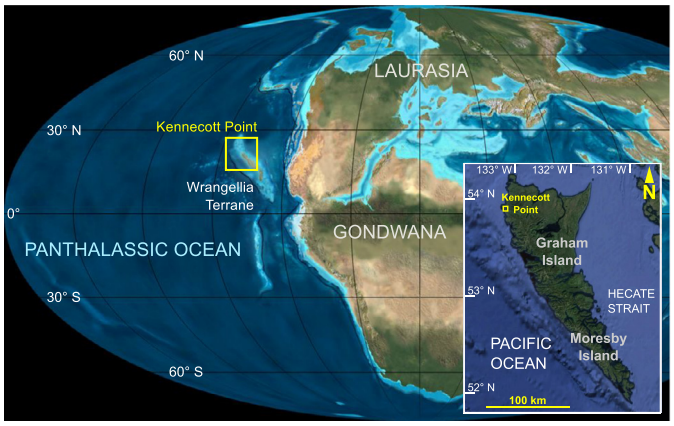

Fig. 2. Late Triassic global paleogeography. The location of the Wrangellia Terrane (and Kennecott Point section) in the Panthalassic Ocean is approximate. Base map courtesy of Ron Blakey, Colorado Plateau Geosystems. Inset shows Haida Gwaii, with the modern location of the Kennecott Point section on the northwestern shore of Graham Island highlighted (from Google Earth Pro).

Japan (Carter and Hori, 2005), suggesting that the Kennecott Point depositional environment was generally representative of open-ocean conditions.

The Kennecott Point section is located on the western coast of Graham Island, the northern major island of the Haida Gwaii (Fig. 2; Longridge et al., 2007). The lowermost 12 m of the section (Fig. 3) is assigned to the Norian Peril Formation, which consists of bituminous calcareous shale and siltstone containing abundant concentrations of the flat bivalve genus *Monotis* (Ward et al., 2004). The majority of the section (128 m) belongs to the Sandilands Formation (Tipper et al., 1991), which is composed of organic-rich silicified siltstones and shales, with interbeds of fine turbiditic and thin tuffaceous sandstones. This unit ranges in age from the earliest Rhaetian to the latest Sinemurian (Longridge et al., 2007). The present study focuses on the interval from the uppermost Norian to the uppermost Hettangian.

The Kennecott Point section has been the subject of extensive geochemical work, including organic carbon (Ward et al., 2001, 2004; Williford et al., 2007) and sulfur isotope studies (Williford et al., 2009). These revealed a minor (~2‰) negative carbon isotope excursion corresponding to the ETME interval, followed by a major (~6‰), prolonged, positive excursion in the Hettangian. Sulfur isotopes show two discreet positive excursions, toward values suggesting quantitative sulfate reduction (Williford et al., 2009), in the 15 m interval between the disappearance of abundant heteromorph ammonoids of the genus *Choristoceras* and the appearance of Jurassic radiolarians. A more sustained positive excursion, toward similar seawater-sulfate values, is seen in the Hettangian, roughly corresponding in duration to that seen in organic carbon isotopes.

A comprehensive biomarker study of the section by Kasprak et al. (2015) revealed many of the processes associated with the 'greenhouse extinction' model were occurring in the water column immediately before and during the ETME interval. The presence of C_{18-22} aryl isoprenoids and isorenieratane provides unambiguous evidence of photic-zone euxinia during and after the extinction. Other biomarker proxies suggest an increased component of prasinophytes and bacterial phytoplankton in the earliest Jurassic, including cyanobacteria and methanotrophs. Biomarkers for algal productivity show a steady decline through much of the Rhaetian, with two minima preceding the ETME interval.

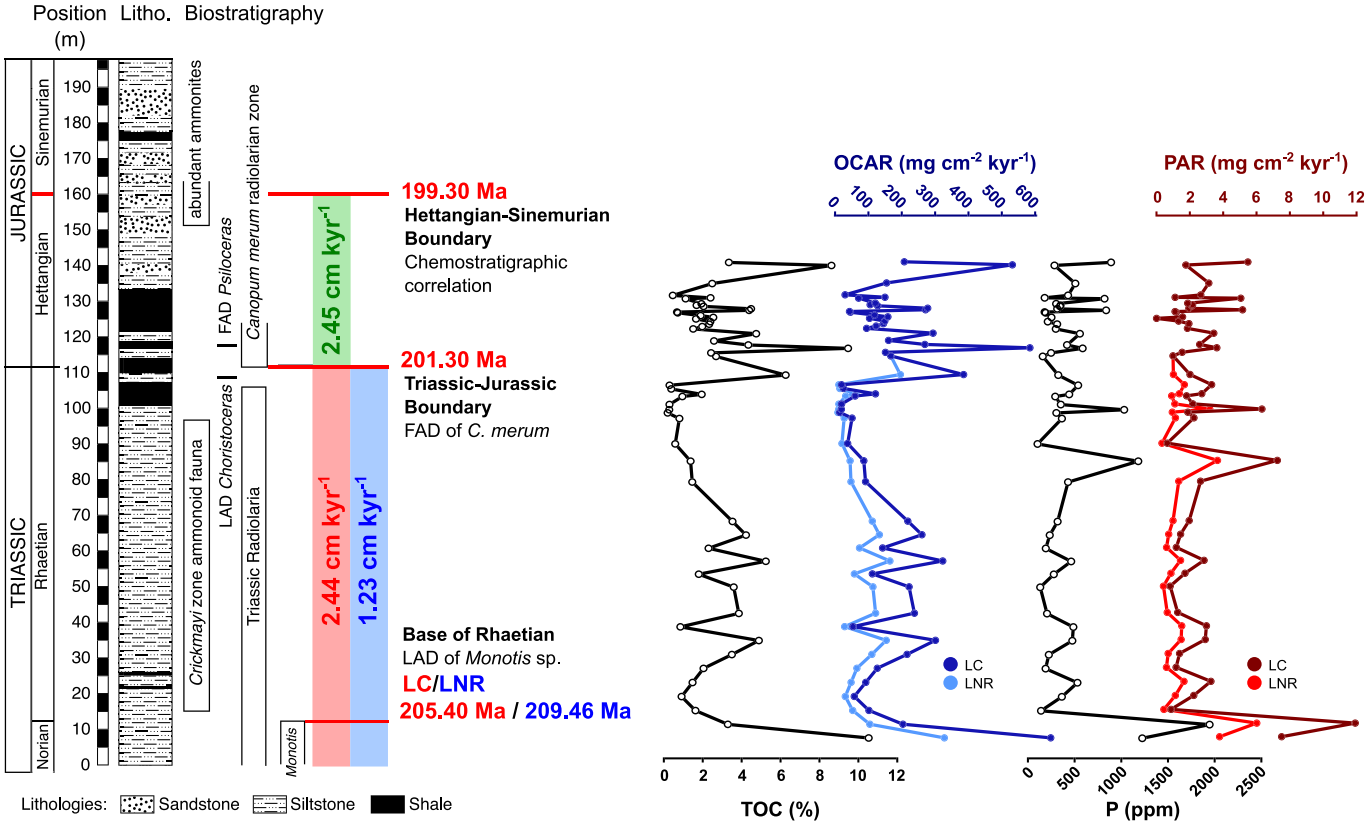

Fig. 3. Stratigraphy of the Kennecott Point section (from Williford et al., 2009). Stage-boundary tie points, as well as the revised position of the Hettangian–Sinemurian boundary (Bartolini et al., 2012), are highlighted in red. Red or blue numbers indicate ages from Gradstein et al. (2012); see text for details of age interpretations. The profiles show concentrations and accumulation rates of two productivity proxies (TOC, P), based on both the long-Carnian (LC) and long-Norian–Rhaetian (LNR) age models of Gradstein et al. (2012). (For interpretation of the references to color in this figure legend, the reader is referred to the web version of this article.)

3. Methods

3.1. Geochemical measurements

A suite of 54 samples was measured for organic nitrogen isotopes at the University of Washington's IsoLab facility, including the 51 samples reported in Kasprak et al. (2015), plus 3 additional samples to better constrain variability in the lower part of the section. These samples were further analyzed for carbon and sulfur concentrations using an Eltra-2000 C-S elemental analyzer at the University of Cincinnati, and a subset of 51 samples was analyzed for elemental composition by X-ray fluorescence spectroscopy (XRF). Details of sample preparation are included in the Supplementary Information.

3.2. Biostratigraphy and age models

The Haida Gwaii sections at Kennecott Point and Kunga Island have been the subject of extensive biostratigraphic study, with both ammonoids and radiolarians being used to establish correlations to other sections worldwide (Guex et al., 2004; Carter and Hori, 2005). Three primary tie points representing stage boundaries were used to establish sedimentation rates in this study (Fig. 3). The first is the extinction of the previously abundant bivalve genus *Monotis*, an important marker for the Norian/Rhaetian (N/R) boundary in high-latitude sections (Krystyn, 2010). The second is the biostratigraphic Triassic–Jurassic boundary (TJB), defined by the first appearance of *Psiloceras spelae* at the GSSP at Kuhjoch, Austria. While *P. spelae* is absent at Kennecott Point, the interval between the first appearance of Jurassic radiolarians (with *Canoptum merum* being a key index fossil; Carter and Hori, 2005) and the appearance of *P. pacificum* is taken to be equivalent to the *spelae* Zone in the Panthalassic realm (Longridge et al., 2007), and we will therefore identify the TJB at Kenencott Point at the first appearance of *C. merum*. The Hettangian/Sinemurian boundary was initially placed at the first appearance of the Badouxia zone ammonoid genus *Vermiceras* (Williford et al., 2007) estimated to occur 190 m above the base of the Kennecott Point section based upon a correlation of earlier biostratigraphy at Kennecott Point by Tipper et al. (1991) with the global stratotype for the basal Sinemurian (Bloos and Page, 2002). Newer ammonoid biostratigraphy from Kennecott Point (Longridge et al., 2007) and a more recent and comprehensive reassessment of Triassic–Jurassic bio- and carbon isotope stratigraphy, including new carbon isotope data from the New York Canyon (Nevada, USA) sections (Bartolini et al., 2012), suggests that the Hettangian/Sinemurian boundary should be placed approximately 160 m above the base of the section at Kennecott Point. We accept that revision here. Dates from Gradstein et al. (2012) are used for all of these stage boundaries.

Although the disappearance of monotid bivalves is understood as defining the N/R boundary, the age of this boundary depends on two competing interpretations of late Triassic stratigraphy. The long-Carnian (LC) model places the N/R boundary later in the Triassic, at 205.4 Ma, whereas the long-Norian–Rhaetian (LNR) model places the N/R boundary earlier, at 209.5 Ma (see Gradstein et al., 2012, for a discussion of the evidence supporting each of these models). In this study, we calculate sedimentation rates using both models, offering a sensitivity test for paleoproductivity estimates to uncertainties in age control. However, chronostratigraphic work since the publication of Gradstein et al. (2012) has tended to support a Norian–Rhaetian boundary age consistent with the long-Carnian model (Maron et al., 2015).

3.3. Sedimentary flux and primary productivity calculations

Concentrations of sedimentary components were converted into mass accumulation rates (MAR) with the formula:

$$\mathrm{MAR}_i = X_i \times \mathrm{LSR} \times \mathrm{DBD} \quad (1)$$

where X is the proportion by weight (hence a dimensionless variable) of sedimentary component i, LSR is the linear sedimentation rate (in $\mathrm{cm\,kyr^{-1}}$), DBD is the dry bulk density of the sediment (in $\mathrm{g\,cm^{-3}}$), and MAR has units of $\mathrm{g\,cm^{-2}\,kyr^{-1}}$. Note that LSR × DBD equals the mass accumulation rate of the bulk sediment. LSR was determined between stratigraphic tie points as described in Section 3.2. DBD was assumed equal to 2.5 $\mathrm{g\,cm^{-3}}$ throughout the section, which is a typical average density for indurated sedimentary rocks.

Productivity proxy fluxes were converted to estimates of original primary productivity (Fig. 3) using transform equations from Schoepfer et al. (2015). Equation (2) (Equation (18) of the source paper) is derived from a regression of the relationship between sedimentation rate and the rate of organic carbon preservation in sediments. As such, it attempts to correct for the effect of rapid sedimentation on organic matter preservation:

$$\mathrm{PROD_{prim.}} = 1000 \times \left(10^{4.1} \times \mathrm{TOC}\right)/\mathrm{MAR}^{0.54} \quad (2)$$

where $\mathrm{PROD_{prim.}}$ is primary productivity in units of $\mathrm{mg\,C\,cm^{-2}\,kyr^{-1}}$, TOC is the weight proportion of organic carbon (a dimensionless variable), and MAR is the sediment mass accumulation rate in units of $\mathrm{g\,cm^{-2}\,kyr^{-1}}$ (equivalent to BAR, bulk accumulation rate, in Schoepfer et al., 2015). Our reported productivity results can be converted to units of $\mathrm{g\,C\,m^{-2}\,a^{-1}}$ by dividing the value in $\mathrm{mg\,C\,cm^{-2}\,kyr^{-1}}$ by a factor of 100.

Equations (3) and (4) (Equations (21) and (23) of the source paper) are simple transform functions based on regressions between primary productivity and the accumulation rates of two elemental proxies (TOC and organic P) on a global scale. Due to a weak and inconsistent relationship with productivity, a third elemental proxy investigated by Schoepfer et al. (2015), i.e., barium accumulation rate (BaAR), was not used for primary productivity calculations in the present study.

$$\mathrm{PROD_{prim.}} = \left(10^{8.55} \times \mathrm{OCAR}\right)^{0.43} \quad (3)$$

$$\mathrm{PROD_{prim.}} = \left(10^{3.46} \times \mathrm{PAR}\right)^{1.14} \quad (4)$$

where $\mathrm{PROD_{prim.}}$ is primary productivity in units of $\mathrm{mg\,C\,cm^{-2}\,kyr^{-1}}$, OCAR is the organic carbon accumulation rate, and PAR is the organic phosphorus accumulation rate, both in units of $\mathrm{mg\,cm^{-2}\,kyr^{-1}}$.

Felix (2014) comprehensively reviewed a number of published equations for estimating paleoproductivity from TOC and other sedimentary parameters. To supplement the approaches developed in Schoepfer et al. (2015), we used the two equations that were found to be most reliable by Felix (2014):

$$\mathrm{PROD_{prim.}} = 100 \times (\mathrm{TOC} \times \mathrm{DBD})/\left(0.003 \times \mathrm{LSR}^{0.3}\right) \quad (5)$$

$$\mathrm{PROD_{prim.}} = 531 \times (\mathrm{TOC} \times \mathrm{DBD})^{0.71} \times \mathrm{LSR}^{0.07} \times \mathrm{WD}^{0.45} \quad (6)$$

where WD is the water depth of the depositional environment in meters. Given uncertainty regarding depositional water depths at Kennecott Point, we used a range of estimates (200–500 m). A factor of 100 has been inserted in these equations in order to convert productivity estimates to units of $\mathrm{mg\,C\,cm^{-2}\,kyr^{-1}}$. The ultimate source of Equation (5) is Müller and Suess (1979) and that of Equation (6) is Stein (1986).

4. Results

4.1. Nitrogen isotopes

The nitrogen isotope results reported here expand on those reported in Kasprak et al. (2015), with the addition of some additional samples not included in that study (total $n = 54$; Fig. 4). All

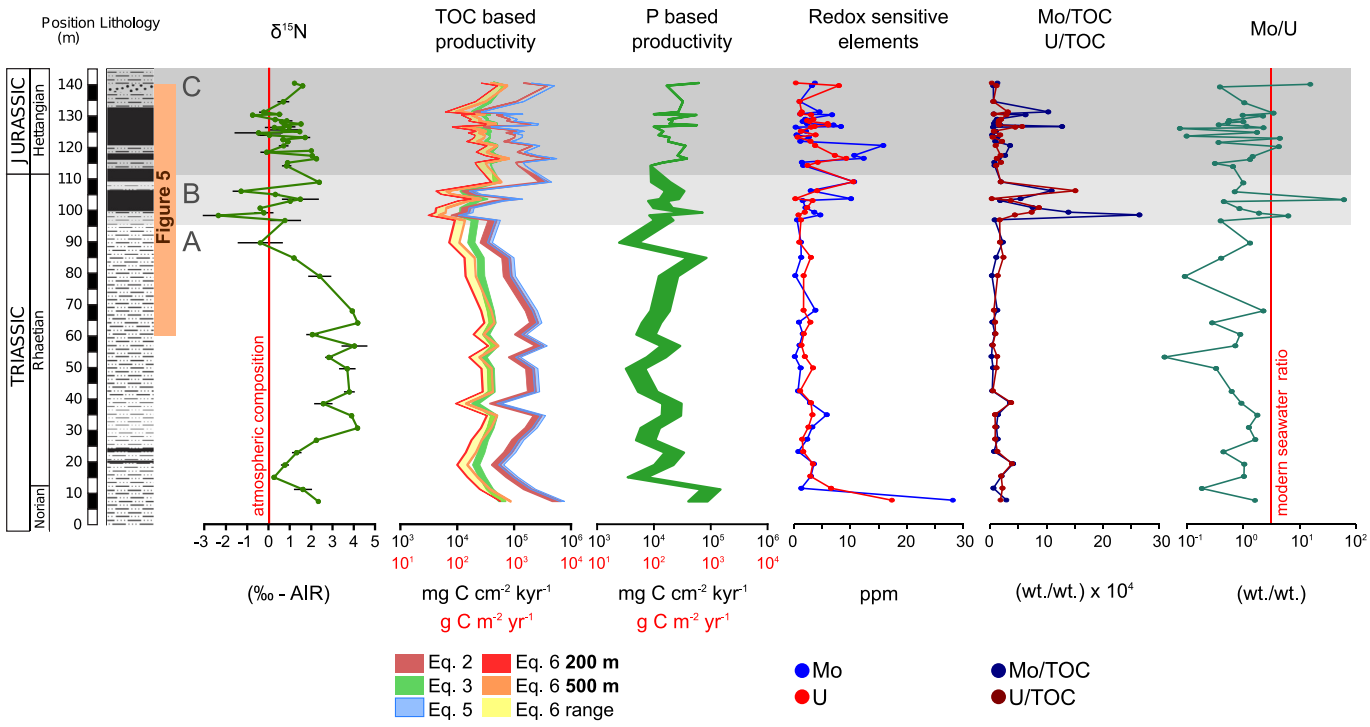

Fig. 4. Stratigraphic trends in δ^{15}N, marine productivity, and redox conditions. Error bars in δ^{15}N column represent 1σ of triplicate measurements, and the vertical red line indicates the δ^{15}N of air. This nitrogen isotope curve supersedes that of Kasprak et al. (2015), which contains several stratigraphically misplaced points. Width of the colored band for productivity estimates indicates range of values calculated using LC and LNR age models. Equations (2), (3), and (4) are from Schoepfer et al. (2015); Equation (5) is from Müller and Suess (1979); Equation (6) is from Stein (1986). Yellow shaded band shows range of values for water depths between 200 and 500 m. Vertical red line in Mo/U panel indicates the Mo/U weight ratio in modern seawater (from Algeo and Tribovillard, 2009). Interval A represents the pre-crisis interval, B the early crisis interval, and C the main crisis interval. Stratigraphic column modified from Williford et al. (2009). Orange highlighted field corresponds to interval shown in Fig. 5. (For interpretation of the references to color in this figure legend, the reader is referred to the web version of this article.)

isotope measurements, as well as the sedimentary nitrogen concentrations measured by elemental analysis during the nitrogen isotope measurements, are reported in Table S1. Possible diagenetic effects on nitrogen isotopes are assessed in the Supplementary Information and Fig. S2.

The average δ^{15}N for the Kennecott Point section is +1.3‰ (s.d. = 1.4‰). The section begins with a prolonged negative excursion, from the lowermost measurement of +2.3‰ in the Norian (Fig. 4) to a minimum value of +0.2‰ in the lowermost Rhaetian. There follows an interval of relative stability encompassing most of the Rhaetian, in which δ^{15}N values range from +2 to +4‰ (mean = +3.4‰, s.d. = 0.8‰, $n = 11$). This is interrupted first by a gradual decline toward the atmospheric value of 0‰, then by a pair of negative excursions, beginning approximately 14 m below the TJB, with the first reaching a minimum value of −2.4‰ (newly reported in this study) and the second reaching a minimum of −1.3‰ approximately 8 m higher up (Fig. 4). These two minima are separated by a brief return to more positive values (local maximum = +1.5‰). The δ^{15}N values in the Hettangian range from −0.8 to +2.2‰, with a mean of +0.8‰ (s.d. = 0.7‰). While the pattern suggests rapid variability, this may partially be the effect of high sampling resolution in this interval, and nitrogen isotope values display no consistent long-term trend in the Hettangian.

4.2. Redox proxies

Molybdenum is highly sensitive to redox conditions in marine environments, and its concentration in marine sediments is a widely used redox proxy (Algeo and Tribovillard, 2009). The highest measured molybdenum concentration (28 ppm) is in the lowermost sample, from the Norian-age Peril Formation (Fig. 4). Mo concentrations drop off quickly in the Sandilands Formation, with relatively low and consistent values throughout the Rhaetian, typically below 5 ppm (mean = 2.7 ppm, s.d. = 2.7). Molybdenum concentrations gradually increase toward higher values (10–20 ppm) in the uppermost Rhaetian, and peak in the lower Hettangian, centered around the first appearance of psiloceratid ammonoids (Fig. 4). Mo values generally return to <5 ppm above this spike, with minor excursions to values >5 ppm at 126.90 and 130.32 m.

Uranium is also a useful proxy for redox conditions in marine environments (Algeo and Tribovillard, 2009). The pattern of uranium concentrations in the section closely tracks the pattern seen in molybdenum, with a maximum value in the Peril Formation (17 ppm; Fig. 4). Uranium remains low (<5 ppm) throughout the Rhaetian (mean = 2.4 ppm, s.d. = 1.9). Spikes to U concentrations above 5 ppm are seen in the lower Hettangian, coinciding with those in Mo, with maxima at 116.45 and 127.07 m. Mo and U concentrations are correlated with an $r^2 = 0.52$ throughout the section.

4.3. Productivity proxies

The most straightforward proxy for productivity is organic carbon, which exhibits a wide range of concentrations in the Kennecott Point section (Fig. 3). The maximum value of TOC (10.5%) occurs in the Peril Formation. Values are highly variable in the lower Rhaetian (mean = 2.1%, s.d. = 1.7%), but typically below 5%. Low values, consistently below 2%, are seen in the uppermost Rhaetian, between 100 and 106 m. TOC is even more variable in the Hettangian, ranging from 0.4 to 9.5% (mean = 2.9%, s.d. = 2.2%), with high values between 114.20 and 121.88 m and maxima at 127.07 and 139.61 m.

Phosphorus, as a major nutrient, has also been used as a productivity proxy, and recent studies have supported its applicability in paleomarine productivity studies (Schoepfer et al., 2015). P concentrations are fairly low throughout the section, never ex-

ceeding 2000 ppm (Fig. 3). Phosphorus values are notably elevated in the Norian Peril Formation (above 1000 ppm), but remain below 500 ppm throughout most of the lower Rhaetian (mean = 312 ppm, s.d. = 136 ppm), before spiking in the upper Rhaetian and remaining elevated and variable thereafter. Several samples above 99 m, in the latest Rhaetian and Hettangian, show P concentrations above 750 ppm (Fig. 3).

4.4. Sediment productivity proxy fluxes

The sedimentary fluxes of productivity proxies were calculated by multiplying proxy concentrations by bulk sediment MAR. The results obtained vary according to the age model used (Fig. 3), but these differences are relatively minor, and consistent stratigraphic patterns are evident. The organic carbon accumulation rate (OCAR) is high, >300 mg cm^{-2} kyr^{-1}, in the lowermost, Norian sample but drops off to consistently low values in the uppermost Norian and Rhaetian, with very low values (<100 mg cm^{-2} kyr^{-1}) seen in the uppermost Rhaetian above 80 m. Values are generally higher in the Hettangian.

Phosphorus accumulation rates (PAR) are consistently lower than those seen in organic carbon. PAR values are elevated in the Norian Peril Formation, consistently >3 mg cm^{-2} kyr^{-1} (Fig. 3). PAR is depressed throughout the lower Rhaetian below 80 m, being <2 mg cm^{-2} kyr^{-1} regardless of the age model used. Unlike OCAR, no uppermost Rhaetian minimum is observed, and in fact PAR shows a number of positive spikes beginning at ~80 m in the upper Rhaetian. Uppermost Rhaetian and Hettangian values are highly variable, but reach values >5 mg cm^{-2} kyr^{-1} during several local maxima in the Hettangian (Fig. 3).

4.5. Quantitative paleoproductivity

Separate estimates of primary productivity were calculated for each combination of equation and age model, but due to the similarity of the various age models and large error associated with productivity estimates, only general trends will be described here.

Applying Equations (2) and (5) produced generally quite high paleoproductivity estimates, values above 300,000 mg C cm^{-2} kyr^{-1} in the uppermost Norian and generally above 100,000 mg C cm^{-2} kyr^{-1} during the pre-extinction Rhaetian (Fig. 4). A substantial decrease in productivity, to a minimum below 50,000 mg C cm^{-2} kyr^{-1}, is seen in the uppermost Rhaetian above 100 m. Estimated productivity increases in the Hettangian, reaching a value above 300,000 mg C cm^{-2} kyr^{-1} again at 116.45 m. Estimates are highly variable throughout the remainder of the section, but generally similar to values in the Rhaetian, i.e., above 100,000 mg C cm^{-2} kyr^{-1}.

Equation (3), which does not attempt to explicitly correct for preservation effects, produces relatively consistent paleoproductivity estimates throughout the uppermost Norian and most of the Rhaetian, centered around a value of 40,000 mg C cm^{-2} kyr^{-1} (Fig. 4). As with the Equation (2) results, a productivity minimum is observed between 100 and 106 m, with values centered around 12,000 mg C cm^{-2} kyr^{-1}. Apparent productivity values quickly recover in the Hettangian, generally being above 30,000 mg C cm^{-2} kyr^{-1}. Values estimated using the Stein (1986) equation (Eq. (6)) yield comparable estimates to Equation (3), overlapping throughout the majority of the Rhaetian (Fig. 4). The minimum productivity values seen during the latest Rhaetian are low when estimated with Equation (6), especially if the water depth is assumed to be 200 m, reaching their lowest point at <4000 mg C cm^{-2} kyr^{-1}.

Equation (4), which is based on PAR, yields some extreme variation in the lowest part of the section, dropping quickly from a Norian value around 100,000 mg C cm^{-2} kyr^{-1} to a minimum below

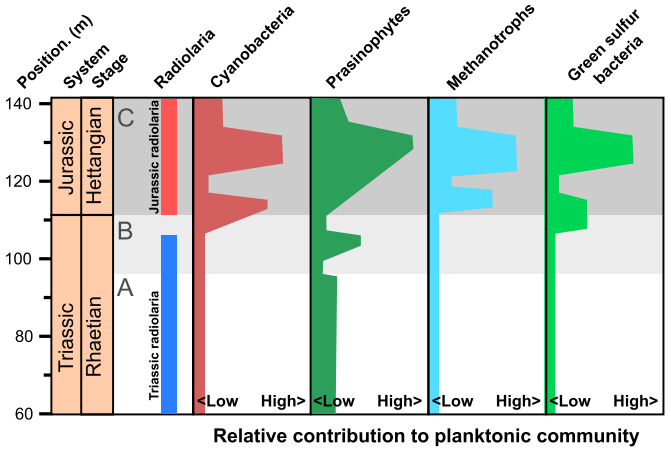

Fig. 5. Generalized stratigraphic trends in planktonic community components across the ETME interval, from 60 to 140 m. Highlighted intervals A, B, and C correspond to those in Figs. 4 and 6. Radiolarian assemblages ranges from Ward et al. (2001), and biomarker evidence for bacterioplankton from Kasprak et al. (2015).

10,000 mg C cm^{-2} kyr^{-1} (Fig. 4). Estimated productivity is more consistent thereafter, centered around 10,000 mg C cm^{-2} kyr^{-1} during most of the Rhaetian. Productivity rises quickly in the uppermost Rhaetian to values above 30,000 mg C cm^{-2} kyr^{-1}, and with some exceptions remains within that range throughout the remainder of the Hettangian.

5. Discussion

5.1. Secular N isotope variation

After the extinction of *Monotis*, Rhaetian δ^{15}N values are fairly stable, ranging from ~ + 2 to +4‰, consistent with the average values seen in greenhouse intervals of Earth history (Algeo et al., 2014), and likely representing the nitrogen cycle in a stable greenhouse mode. Although lower than the modern ocean-surface δ^{15}N average of ~ + 5.5‰, sedimentary δ^{15}N values were sufficiently enriched above the atmospheric value of 0‰ to suggest that water-column denitrification operated, and that some of this nitrogen was subsequently recycled upward into the photic zone. Nitrogen isotope ratios shift in a negative direction in the upper Rhaetian (Fig. 4). These minima reflect the onset of environmental stresses that would ultimately lead to the ETME. This interval coincided with an increasing contribution of prasinophytes and green algae as well as cyanobacteria (Fig. 5; Kasprak et al., 2015), and it is likely that the negative shifts reflect increased inputs of ^{15}N-depleted nitrogen by N-fixing diazotrophs.

Following the first appearance of *Canoptum merum*, nitrogen isotope values return to relative stability, averaging between 0‰ and +1‰, with some excursions to negative values (Fig. 4). This new δ^{15}N equilibrium is considerably lower than that seen in the Rhaetian, even though it coincided with a recovery in apparent productivity to approximately Rhaetian levels, suggesting that sufficient nitrogen was available to maintain phytoplankton productivity. This transition also coincided with the first appearance of substantial isorenieratane, as well as biomarker evidence for methanotrophs (Fig. 5; Kasprak et al., 2015). These indicators suggest a largely bacterial plankton community dependent on the presence of reduced species (H_2S, CH_4) in the shallow, photic ocean, indicating a shoaling of the stable chemocline that had existed during the latest Triassic. Under these circumstances, an upward flux of ammonium would be expected along with these other reduced species, favoring the proliferation of prasinophytes (Prauss, 2007). Continuous upwelling of ammonium, as well as re-

cycling of ammonium by the photic-zone planktonic community, would have maintained the $\delta^{15}N$ of plankton biomass at $\delta^{15}N$ values near 0‰, although nitrification of ammonium could potentially have induced some enrichment of the NH_4^+ pool (Higgins et al., 2012).

5.2. Productivity history of the study section

Productivity estimates based on the transform equations of Schoepfer et al. (2015) show considerable stratigraphic variation that can be related to other geochemical signals in the section (Fig. 4). Regionally averaged, long-term productivity values in the modern ocean (Longhurst et al., 1995) range from approximately 6000 to 79,000 mg C cm^{-2} kyr^{-1}, a span that incorporates the majority of productivity estimates generated from Equations (3) and (4).

Values derived from Equation (2) are quite high, above 100,000 mg C cm^{-2} kyr^{-1} throughout much of the Rhaetian, suggesting that the equation may be overcorrecting for the low sedimentation rates in this depositional system, although the equation of Müller and Suess (1979) yields very similar productivity estimates to Eq. (2) (Fig. 4). Productivity estimates from the Stein (1986) equation vary somewhat depending on the water depth used, but are in better agreement with the lower estimates generated by Equations (3) and (4). Use of the LC versus the LNR age model does not have major implications for carbon-based productivity estimates, with the largest offset between the age models being seen in the phosphorus-based productivity estimates calculated from Equation (4) (Fig. 4).

Apparent productivity during the pre-crisis Rhaetian interval ("baseline") varies depending on which equation is used but is secularly uniform, suggesting stable environmental conditions. Estimates of Rhaetian productivity derived from Equation (3), and the Stein (1986) equation (Eq. (6)), are centered around 25,000 mg C cm^{-2} kyr^{-1}, comparable to values seen in the modern subarctic Pacific or the western margin of South America (Longhurst et al., 1995). Values derived from Equation (4), typically around 10,000 mg C cm^{-2} kyr^{-1} or slightly higher, are comparable to those in subtropical gyres at higher latitudes in the Pacific Ocean and at the equatorial divergence (Longhurst et al., 1995). While the paleoproductivity estimates generated using these transform functions are imprecise, they are typical of environments with a mixed layer deeper than that of low-productivity tropical gyres, although lower than those of the most intensely productive coastal upwelling systems. Given the low-latitude location of the Wrangellia Terrane during the latest Triassic (Fig. 2; Jones et al., 1977; Carter and Hori, 2005), these estimates suggest somewhat elevated ocean-surface nutrient levels due to upwelling, caused either by Panthalassic equatorial divergence or by the bathymetry of the Wrangellia Terrane margin.

Aside from a minimum in calculated paleoproductivity around the Norian–Rhaetian boundary, the principal feature of the productivity curves is a decline through the uppermost Rhaetian (Fig. 4), corresponding to the productivity "collapse" described by Ward et al. (2001). This interval exhibits two minima that yield similar estimates for all equations and age models, ranging from 10,000 to 20,000 mg C cm^{-2} kyr^{-1}, separated by a brief excursion toward higher productivity. Hettangian productivity estimates generally appear to represent a return to values similar to the pre-crisis Rhaetian "baseline" regardless of which equation is used (Fig. 4), despite biomarker evidence that the planktonic community included exotic components that were not present in the Rhaetian, such as green sulfur bacteria and methanotrophs (Kasprak et al., 2015).

5.3. Relationship between N isotopes, productivity, and redox conditions

Negative excursions in $\delta^{15}N$ correspond well with declining carbon-based productivity estimates (Fig. 4). The correspondence between $\delta^{15}N$ and productivity estimates based on phosphorus is not as strong (but the Norian–Rhaetian productivity minimum is still evident). An increased component of nitrogen fixation coinciding with minima in productivity likely reflects the limitation of primary productivity by nitrogen availability in these intervals. Although evidence for cyanobacterial nitrogen fixation in the latest Rhaetian and early Hettangian does suggest a homeostatic response to low N availability, the observation that pre-crisis Rhaetian levels of productivity were not maintained suggests that the cyanobacterial response to low-N conditions was inadequate to restore a Redfieldian balance with other nutrients until another source of exogenous nitrogen (deepwater NH_4^+) began to impinge on the photic zone. Using the terminology of Tyrrell (1999), nitrogen was the proximal limiting nutrient on phytoplankton productivity under these circumstances, whereas phosphorus or another micronutrient was the ultimate limiting factor. Low N availability during the Rhaetian–Hettangian transition may have reduced productivity below baseline levels on a geologically significant timescale, possibly due to the energetic burden of diazotrophy and the corresponding competitive advantage of phytoplankton using regenerated NH_4^+ (Tyrrell, 1999).

Alternatively, the decline in the organic carbon burial flux during the Rhaetian–Hettangian transition may reflect a decrease in export productivity rather than primary productivity (cf. Schoepfer et al., 2015). In a steady-state system, the fraction of fixed carbon that is exported from the photic zone is expected to equal the fraction of productivity supported by exogenous nutrient inputs (the f-ratio; Eppley and Peterson, 1979), which was potentially minimal in a stratified and nitrogen-limited environment. However, necromass from a bacterially-dominated phytoplankton would tend to decompose quickly in the surface mixed layer, keeping nutrients available within a short microbial loop (Luo et al., 2014). If small zooplankton abundance was also depressed in this interval (as suggested by low abundances of heteromorph ammonoids, which likely fed on small zooplankton), export of carbon in the form of dead plankters and fecal pellets may also have been suppressed, leading to decreased carbon export to the sediment.

Proxies for redox conditions show a consistent stratigraphic pattern (e.g., a maximum in the Norian; Fig. 4) that has a significant relationship with TOC ($r^2 = 0.36$ for Mo, $r^2 = 0.55$ for U; Fig. S1). This may reflect a shared underlying control between TOC and the productivity proxies, such as reducing bottom water conditions enhancing TOC preservation, or biological oxygen consumption being the primary cause of bottom water anoxia. Both of these hypotheses assume that trace metal concentrations are accurately recording intervals of low oxygen in the water column; however, if the flux of organic material to the sediment, independent of the redox environment, is the main vector by which trace metals are accumulated in sediments (e.g., Algeo and Lyons, 2006), then redox proxy profiles may be largely tracking TOC accumulation. Normalizing trace element concentrations to TOC (Algeo and Lyons, 2006) may allow us to distinguish a superimposed redox signal, controlled by changes in the particle reactivity of dissolved trace metals and the long-term sequestration potential of trace elements in sedimentary sulfides.

TOC normalization removes much of the variability seen in the redox proxy profiles (Fig. 4), indicating a fairly consistent redox environment through the latest Norian and Rhaetian, although with minor shifts toward more reducing conditions nonetheless evident in the lower Rhaetian at 19.16 and 38.64 m. Normalized redox proxies are consistently elevated beginning in the uppermost Rhaetian at 99.30 m, preceding the extinction of Triassic radiolaria

and biomarker evidence for photic-zone euxinia, but coinciding with the onset of increased stratification, as recorded in the gammacerane index and reducing bottomwater conditions recorded by the homohopane and C_{28} disnorhopane indices (Kasprak et al., 2015). If this interval does indeed represent a minimum in productivity, then it records an inverse relationship between productivity and dysoxia in the water column. This pattern implies that low-oxygen conditions resulted from stratification of the water column rather than biological oxygen demand, a condition that could have contributed to low nutrient availability and productivity in the surface ocean.

Interestingly, this evidence for reducing conditions is not seen in other Panthalassic sections. While evidence for anoxia is widespread in Tethyan/proto-Atlantic settings (Kasprak et al., 2015, and references therein), no evidence for euxinia has been found at the Triassic–Jurassic boundary from the pelagic Mino-Tamba Terrane of Japan (Wignall et al., 2010). The Kennecott Point section contains a diverse radiolarian fauna, suggesting basinal restriction is not responsible for the localization of anoxia. Instead, euxinic conditions may have developed most strongly in a mid-water oxygen minimum, with the abyssal ocean remaining largely oxic to suboxic (Algeo et al., 2011).

5.4. Stratification, nutrient cycling, and mass extinction

By combining nitrogen isotope, productivity proxy, and redox proxy data, supplemented by the biomarker data published in Kasprak et al. (2015), an integrated model of oceanographic conditions across the Triassic–Jurassic boundary at Kennecott Point can be developed, with two clear phases of the end-Triassic extinction recognizable (Fig. 6).

The first phase, beginning in the latest Rhaetian, is associated with enhanced nitrogen fixation in the photic zone, decreased productivity, evidence for enhanced particle reactivity of redox-sensitive elements, and elevated Mo/U ratios, suggesting euxinic conditions already developing in the bottom water (Fig. 4; Algeo and Tribovillard, 2009). Biomarker data indicate an increasing predominance of green algae and cyanobacteria, suggesting a phytoplankton stressed by limited nutrient availability but still able to support a diverse radiolarian assemblage. This phase likely corresponded to a period of intense density stratification of the oceanic water column, possibly due to strong climatic warming associated with the CAMP flood basalt eruptions (McElwain et al., 1999). However, the lack of biomarkers for green sulfur bacteria suggests that the chemocline generally remained below the base of the photic zone. The sparseness in this interval of *Choristoceras*, which as a heteromorph ammonoid was likely a vertical migrant (Ward, 1979), may reflect increasingly stressed conditions at thermocline water depths. There is some indication that similar conditions, with low productivity and enhanced nitrogen fixation, prevailed around the Norian–Rhaetian boundary, and may have been related to the increasing dwarfism and local disappearance of monotid bivalves (Ward et al., 2004).

The second phase corresponds to the Triassic–Jurassic boundary, as well as to the appearance of green sulfur bacteria (i.e., isorenieratane) and their zooplankton grazers (i.e., gammacerane), suggesting a breakdown or shoaling of the chemocline, allowing euxinic waters into the photic zone (Fig. 6; Kasprak et al., 2015). Although this seems to have been the fatal blow for Triassic radiolarians and ammonoids, it corresponds to a modest recovery in productivity (Figs. 3, 4). Sedimentary nitrogen isotopes, although remaining low, show a consistency not seen in the uppermost Rhaetian (Fig. 4). This consistency suggests a new source of exogenous nitrogen, e.g., the introduction of deepwater ammonium into the photic zone, where it could support the productivity of those phytoplankton able to survive in the euxinic earliest Jurassic environment. This proliferating planktonic community, dependent on reduced species (H_2S, CH_4, NH_4^+), would have fueled the diversification of Jurassic radiolaria, as a food source and, potentially, through the development of symbiotic relationships with radiolarians.

5.5. Timing and causality of Triassic–Jurassic transition events

Blackburn et al. (2013) tied the end-Triassic extinction horizon (as defined by a turnover in sporomorphs) to the initial onset of extrusive volcanism associated with the Central Atlantic Magmatic Province, and dated the event at 201.564 Ma. The stratified pre-extinction phase in the Kennecott Point section began ~10 m below the extinction of Triassic radiolarians, suggesting that either the onset of these conditions preceded the initial eruption of the CAMP, possibly by over half a million years, and cannot be causally linked to it, or that the sporomorph turnover that defines the terrestrial ETME was not coincident with the marine extinction event, with marine environments potentially having been better buffered against the short-term effects of massive volcanism than terrestrial environments.

Using the long-term average Rhaetian sedimentation rates of the LC and LNR age models (Fig. 3), this stressed interval had a duration of ~400 to 800 kyr, which coincides reasonably well with both the duration of the CAMP eruptions (~600 kyr, Blackburn et al., 2013) and the duration of the ecological disturbance seen in other Panthalassic sections (Ritterbush et al., 2014; Corsetti et al., 2015). However, this is orders of magnitude longer than the residence time of nitrogen in the ocean (~3000 yr; Gruber, 2008), suggesting that the marine nitrogen cycle must have settled into a new homeostatic equilibrium during this interval. Sedimentary denitrification during warm intervals of Earth history is associated with low $\delta^{15}N$ values, since it is typically quantitative and has no net fractionation effect (Algeo et al., 2014), however the Late Triassic world had been free of permanent polar ice for millions of years, and it is difficult to associate this event with an increase in flooded continental area that would have driven an increase in sedimentary denitrification.

If this event does represent an increase in water-column denitrification, then the associated decline in productivity would be among the first evidence for limitation of marine productivity by nitrogen availability on geologically significant timescales. Phosphorus has typically been viewed as the ultimate biolimiting nutrient (Tyrrell, 1999), but the characteristic timescale over which these forms of nutrient limitation can operate has not been determined. Here, we report limitation of productivity by low N availability in the open ocean over several hundred thousand years. However, it is worth noting that apparent nitrogen limitation is limited to a crisis interval and likely related to the eruption of the CAMP – it may not be a pervasive feature of greenhouse environments as has been hypothesized (Saltzman, 2005), nor do we see evidence for a "shutdown" of the N cycle (Kidder and Worsley, 2010), even as euxinia impinged on the photic zone and caused mass extinction during the ETME crisis.

6. Conclusions

The Kennecott Point section preserves evidence for a disturbance of the open marine nitrogen cycle in the 400–800 kyr immediately preceding the biostratigraphic Triassic–Jurassic boundary. This negative excursion in sedimentary nitrogen isotopes represents a deviation from the Rhaetian "baseline" greenhouse state, and likely represents an enhanced component of cyanobacterial N fixation from the atmosphere, in response to nitrogen limitation. This interval coincides with a minimum in primary or export

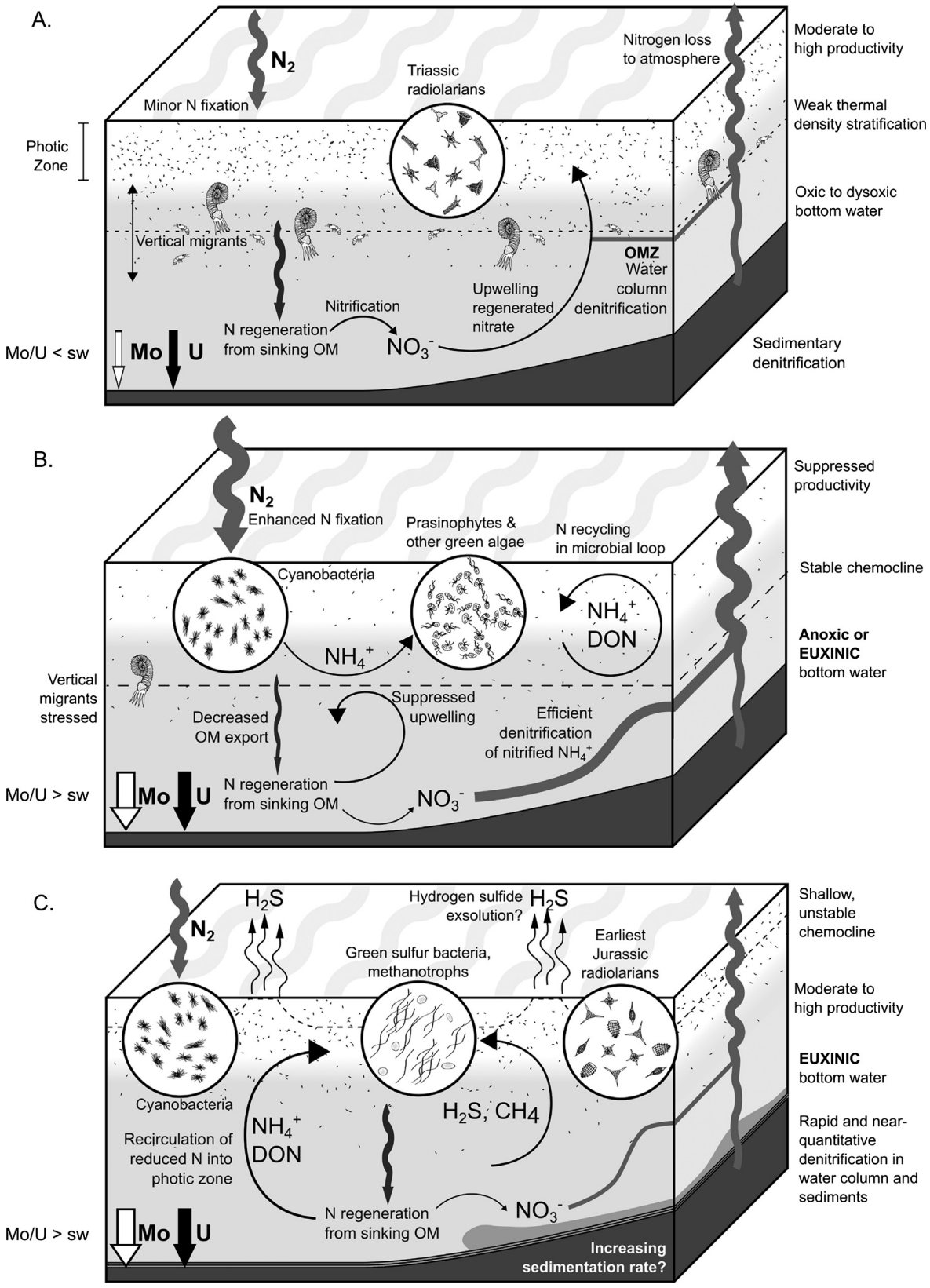

Fig. 6. Integrated model of nutrient cycling and marine productivity during the Late Triassic at Kennecott Point. (A) Pre-crisis greenhouse conditions (most of Rhaetian). (B) Stratified, nitrogen-limited conditions (Norian–Rhaetian boundary(?) and latest Rhaetian). (C) Crisis interval with influx of euxinic waters into the photic zone (ETME and early Hettangian). Letters correspond to intervals in Figs. 4 and 5.

production, as estimated from the organic carbon content and sedimentation rate, suggesting that low nitrogen availability limited productivity before and during the ETME, the first such evidence for nitrogen limitation over geologically significant timescales during a mass extinction interval. This interval was characterized by the development of stable density stratification below the base

of the photic zone, and euxinic conditions in the bottom water; the decreasing abundance of heteromorph ammonoids, likely water column vertical migrants, may be due to ecological stress in the thermocline. The appearance of Jurassic radiolarians coincides with evidence for a recovery in productivity, potentially related to the introduction of regenerated deep-water ammonium as a new exogenous nitrogen source as the chemocline began to impinge on the photic zone in the earliest Jurassic.

Acknowledgements

The authors would like to express our gratitude to the Haida First Nation of Haida Gwaii for access to the sampling locality. We would also like to thank the University of Washington Department of Earth and Space Sciences for funding much of this work. We would like to especially thank the staff of the UW IsoLab for their help with isotope measurements. KHW acknowledges support from the National Aeronautics and Space Administration for work performed at the Jet Propulsion Laboratory, California Institute of Technology. TJA gratefully acknowledges support from the Sedimentary Geology and Paleobiology program of the U.S. National Science Foundation (EAR-1053449), the NASA Exobiology program (NNX13AJ1IG), and the China University of Geosciences-Wuhan (programs GPMR201301 and BGL21407).

Appendix A. Supplementary material

Supplementary material related to this article can be found online at http://dx.doi.org/10.1016/j.epsl.2016.06.050.

References

Algeo, T.J., Lyons, T.W., 2006. Mo-total organic carbon covariation in modern anoxic marine environments: implications for analysis of paleoredox and paleohydrographic conditions. Paleoceanography 21 (1), 1–23.

Algeo, T.J., Tribovillard, N., 2009. Environmental analysis of paleoceanographic systems based on molybdenum–uranium covariation. Chem. Geol. 268, 211–222.

Algeo, T.J., Twitchett, R.J., 2010. Anomalous Early Triassic sediment fluxes due to elevated weathering rates and their biological consequences. Geology 38, 1023–1026.

Algeo, T.J., Kuwahara, K., Sano, H., Bates, S., Lyons, T., Elswick, E., Hinnov, L., Ellwood, B., Moser, J., Maynard, J.B., 2011. Spatial variation in sediment fluxes, redox conditions, and productivity in the Permian–Triassic Panthalassic Ocean. Palaeogeogr. Palaeoclimatol. Palaeoecol. 308 (1), 65–83.

Algeo, T.J., Meyers, P.A., Robinson, R.S., Rowe, H., Jiang, G.Q., 2014. Icehouse–greenhouse variations in marine denitrification. Biogeosciences 11 (4), 1273–1295.

Allmon, W.D., Martin, R.E., 2014. Seafood through time revisited: the Phanerozoic increase in marine trophic resources and its macroevolutionary consequences. Paleobiology 40 (2), 256–287.

Bartolini, A., Guex, J., Spangenberg, J.E., Schoene, B., Taylor, D.G., Schaltegger, U., Atudorei, V., 2012. Disentangling the Hettangian carbon isotope record: implications for the aftermath of the end-Triassic mass extinction. Geochem. Geophys. Geosyst. 13 (1), Q01007. http://dx.doi.org/10.1029/2011GC003807.

Blackburn, T.J., Olsen, P.E., Bowring, S.A., McLean, N.M., Kent, D.V., Puffer, J., McHone, E., Rasbury, T., Et-Touhami, M., 2013. Zircon U–Pb geochronology links the end-Triassic extinction with the Central Atlantic Magmatic Province. Science 340 (6135), 941–945.

Bloos, G., Page, K.N., 2002. Global stratotype section and Point for the base of the Sinemurian stage (Lower Jurassic). Episodes 25, 22–28.

Brasier, M.D., 1995. Fossil indicators of nutrient levels. 1: eutrophication and climate change. In: Bosence, D.W.J. (Ed.), Marine Palaeoenvironmental Analysis from Fossils. In: Geological Society of London Special Publications, vol. 83, pp. 113–132.

Carter, E.S., Hori, R.S., 2005. Global correlation of the radiolarian faunal change across the Triassic–Jurassic boundary. Can. J. Earth Sci. 42, 777–790.

Corsetti, F.A., Ritterbush, K.A., Bottjer, D.J., Greene, S.E., Ibarra, Y., Yager, J.A., West, A.J., Berelson, W.M., Rosas, S., Becker, T.W., Levine, N.M., 2015. Investigating the paleoecological consequences of supercontinent breakup: sponges clean up in the Early Jurassic. Sediment. Rec. 13 (2), 4–10.

Črne, A.E., Weissert, H., Goričan, Š., Bernasconi, S.M., 2011. A biocalcification crisis at the Triassic–Jurassic boundary recorded in the Budva Basin (Dinarides, Montenegro). Geol. Soc. Am. Bull. 123 (1–2), 40–50.

Eppley, R.W., Peterson, B.W., 1979. Particulate organic matter flux and planktonic new production in the deep ocean. Nature 282, 677–681.

Felix, M., 2014. A comparison of equations commonly used to calculate organic carbon content and marine palaeoproductivity from sediment data. Mar. Geol. 347, 1–11.

Gradstein, F.M., Ogg, J.G., Schmitz, M., Ogg, G. (Eds.), 2012. The Geologic Time Scale 2012 2-Volume Set, vol. 2. Elsevier.

Greene, A.R., Scoates, J.S., Weis, D., Katvala, E.C., Israel, S., Nixon, G.T., 2010. The architecture of oceanic plateaus revealed by the volcanic stratigraphy of the accreted Wrangellia oceanic plateau. Geosphere 6 (1), 47–73.

Gruber, N.G., 2008. The marine nitrogen cycle: overview and challenges. In: Capone, D.G., Bronk, D.A., Mulholland, M.R., Carpenter, E.J. (Eds.), Nitrogen in the Marine Environment, 2nd edn. Elsevier, Amsterdam, pp. 1–50.

Guex, J., Bartolini, A., Atudorei, V., Taylor, D.G., 2004. High-resolution ammonite and carbon isotope stratigraphy across the Triassic–Jurassic boundary at New York Canyon (Nevada). Earth Planet. Sci. Lett. 225, 29–41.

Haggart, J.W., Carter, E.S., Beattie, M.J., Bown, P.S., Inkin, R.J., Kring, D.A., Johns, M.J., McNicoll, V.J., Orchard, M.J., Perry, R.S., Schroder-Adams, C.S., Smith, P.L., Suneby, L.B., Tipper, H.W., Ward, P.D., 2001. Stratigraphy of Triassic/Jurassic boundary strata, Queen Charlotte Islands, British Columbia: potential global system stratotype boundary. In: IGCP 458 Field Meeting. October 13–17, Taunton, UK.

Higgins, M.D., Robinson, R.S., Husson, J.M., Carter, S.J., Pearson, A., 2012. Dominant eukaryotic export production during ocean anoxic events reflects the importance of recycled NH_4^+. Proc. Natl. Acad. Sci. USA 109, 2269–2274.

Housen, B.A., Beck, M.E., 1999. Testing terrane transport: an inclusive approach to the Baja BC controversy. Geology 27 (12), 1143–1146.

Ingall, E.D., Kolowith, L., Lyons, T., Hurtgen, M., 2005. Sediment carbon, nitrogen and phosphorus cycling in an anoxic fjord, Effingham Inlet, British Columbia. Am. J. Sci. 305, 240–258.

Jones, D.L., Silberling, N.J., Hillhouse, J., 1977. Wrangellia – a displaced terrane in northwestern North America. Can. J. Earth Sci. 14 (11), 2565–2577.

Kasprak, A.H., Sepúlveda, J., Price-Waldman, R., Williford, K.H., Schoepfer, S.D., Haggart, J.W., Ward, P.D., Summons, R.E., Whiteside, J.H., 2015. Episodic photic zone euxinia in the northeastern Panthalassic Ocean during the end-Triassic extinction. Geology 43 (4), 307–310.

Kidder, D.L., Worsley, T.R., 2010. Phanerozoic large igneous provinces (LIPs), HEATT (haline euxinic acidic thermal transgression) episodes, and mass extinctions. Palaeogeogr. Palaeoclimatol. Palaeoecol. 295, 162–191.

Krystyn, L., 2010. Decision report on the defining event for the base of the Rhaetian stage. Albertiana 38, 11–12.

Kump, L.R., Pavlov, A., Arthur, M.A., 2005. Massive release of hydrogen sulfide to the surface ocean and atmosphere during intervals of oceanic anoxia. Geology 33, 397–400.

Longhurst, A., Sathyendranath, S., Platt, T., Caverhill, C., 1995. An estimate of global primary production in the ocean from satellite radiometer data. J. Plankton Res. 17 (6), 1245–1271.

Longridge, L.M., Carter, E.S., Smith, P.L., Tipper, H.W., 2007. Early Hettangian ammonites and radiolarians from the Queen Charlotte Islands, British Columbia and their bearing on the definition of the Triassic–Jurassic boundary. Palaeogeogr. Palaeoclimatol. Palaeoecol. 244, 142–169.

Luo, G., Algeo, T.J., Huang, J., Zhou, W., Wang, Y., Yang, H., Richoz, S., Xie, S., 2014. Vertical $\delta^{13}C_{org}$ gradients record changes in planktonic microbial community composition during the end-Permian mass extinction. Palaeogeogr. Palaeoclimatol. Palaeoecol. 396, 119–131.

Maron, M., Rigo, M., Bertinelli, A., Katz, M.E., Godfrey, L., Zaffani, M., Muttoni, G., 2015. Magnetostratigraphy, biostratigraphy, and chemostratigraphy of the Pignola–Abriola section: new constraints for the Norian–Rhaetian boundary. Geol. Soc. Am. Bull. 127 (7–8), 962–974.

McElwain, J.C., Beerling, D.J., Woodward, F.I., 1999. Fossil plants and global warming at the Triassic–Jurassic boundary. Science 285 (5432), 1386–1390.

Müller, P.J., Suess, E., 1979. Productivity, sedimentation rate, and sedimentary organic matter in the oceans—I. Organic carbon preservation. Deep-Sea Res., A, Oceanogr. Res. Pap. 26 (12), 1347–1362.

Prauss, M.L., 2007. Availability of reduced nitrogen chemospecies in photic-zone waters as the ultimate cause for fossil prasinophyte prosperity. Palaios 22 (5), 489–499.

Richoz, S., van de Schootbrugge, B., Pross, J., Puttmann, W., Quan, T.M., Lindstrom, S., Heunisch, C., Fiebig, J., Maquil, R., Schouten, S., Hauzenberger, C.A., Wignall, P.B., 2012. Hydrogen sulphide poisoning of shallow seas following the end-Triassic extinction. Nat. Geosci. 5 (9), 662–667.

Ritterbush, K.A., Bottjer, D.J., Corsetti, F.A., Rosas, S., 2014. New evidence on the role of siliceous sponges in ecology and sedimentary facies development in eastern Panthalassa following the Triassic–Jurassic mass extinction. Palaios 29 (12), 652–668.

Saltzman, M.R., 2005. Phosphorus, nitrogen, and the redox evolution of the Paleozoic oceans. Geology 33 (7), 573–576.

Schoepfer, S.D., Shen, J., Wei, H., Tyson, R.V., Ingall, E., Algeo, T.J., 2015. Total organic carbon, organic phosphorus, and biogenic barium fluxes as proxies for paleomarine productivity. Earth-Sci. Rev. 149, 23–52.

Stein, R., 1986. Surface-water-paleo-productivity as inferred from sediments deposited in oxic and anoxic deep-water environment of the Mesozoic Atlantic

Ocean. In: Degens, E.T. (Ed.), Biogeochemistry of Black Shales. In: Mitteilungen des Geologisch–Palaeontologischen Instituts der Universität Hamburg, vol. 60, pp. 55–70.

Tipper, H.W., Smith, P.L., Cameron, B.E.B., Carter, E.S., Jakobs, G.K., Johns, M.J., 1991. Biostratigraphy of the Lower Jurassic formations of the Queen Charlotte Islands, British Columbia. In: Woodsworth, G.J. (Ed.), Evolution and Hydrocarbon Potential of the Queen Charlotte Basin, British Columbia. Geological Survey of Canada, pp. 203–235. Paper 90-10.

Tyrrell, T., 1999. The relative influences of nitrogen and phosphorus on oceanic primary production. Nature 400, 525–531.

van de Schootbrugge, B., Bachan, A., Suan, G., Richoz, S., Payne, J.L., 2013. Microbes, mud and methane: cause and consequence of recurrent Early Jurassic anoxia following the end-Triassic mass extinction. Palaeontology 56 (4), 685–709.

Ward, P.D., 1979. Functional morphology of Cretaceous helically-coiled ammonite shells. Paleobiology 5 (4), 415–422.

Ward, P.D., Haggart, J.W., Carter, E.S., Wilbur, D., Tipper, H.W., Evans, T., 2001. Sudden productivity collapse associated with the Triassic–Jurassic boundary mass extinction. Science 292, 1148–1151.

Ward, P.D., Garrison, G.H., Haggart, J.W., Kring, D.A., Beattie, M.J., 2004. Isotopic evidence bearing on Late Triassic extinction events, Queen Charlotte Islands, British Columbia, and implications for the duration and cause of the Triassic/Jurassic mass extinction. Earth Planet. Sci. Lett. 224, 589–600.

Whiteside, J.H., Ward, P.D., 2011. Ammonoid diversity and disparity track episodes of chaotic carbon cycling during the early Mesozoic. Geology 39 (2), 99–102.

Wignall, P.B., Bond, D.P., Kuwahara, K., Kakuwa, Y., Newton, R.J., Poulton, S.W., 2010. An 80 million year oceanic redox history from Permian to Jurassic pelagic sediments of the Mino-Tamba terrane, SW Japan, and the origin of four mass extinctions. Glob. Planet. Change 71 (1), 109–123.

Williford, K.H., Foriel, J., Ward, P.D., Steig, E.J., 2009. Major perturbation in sulfur cycling at the Triassic–Jurassic boundary. Geology 37 (9), 835–838.

Williford, K.H., Ward, P.D., Garrison, G.H., Buick, R., 2007. An extended organic carbon-isotope record across the Triassic–Jurassic boundary in the Queen Charlotte Islands, British Columbia, Canada. Palaeogeogr. Palaeoclimatol. Palaeoecol. 244, 290–296.